Turbulence generation by mountain wave breaking in flows with directional wind shear

Article

Accepted Version

Guarino, M. V., Teixeira, M. A. C. and Ambaum, M. H. P. (2016) Turbulence generation by mountain wave breaking in flows with directional wind shear. Quarterly Journal of the Royal Meteorological Society, 142 (700). pp. 2715-2726. ISSN 1477-870X doi: https://doi.org/10.1002/qj.2862 Available at http://centaur.reading.ac.uk/65952/

Published version at: http://onlinelibrary.wiley.com/doi/10.1002/qj.2862/abstract

To link to this article DOI: http://dx.doi.org/10.1002/qj.2862

Publisher: Royal Meteorological Society

Turbulence generation by mountain wave breaking in flows with directional wind shear

Maria-Vittoria Guarino*, Miguel A. C. Teixeira and Maarten H.P. Ambaum

Department of Meteorology, University of Reading, Reading, UK

*Correspondence to: Maria Vittoria Guarino, Department of Meteorology, University of Reading, Earley Gate, PO Box 243, Reading RG6 6BB, UK, E-mail: m.v.guarino@pgr.reading.ac.uk

Mountain wave breaking, and the resulting potential for the generation of turbulence in the atmosphere, is investigated using numerical simulations of idealized, nearly hydrostatic atmospheric flows with directional wind shear over an axisymmetric isolated mountain. These simulations, which use the WRF-ARW model, differ in degree of flow non-linearity and shear intensity, quantified through the dimensionless mountain height and the Richardson number of the incoming flow, respectively. The aim is to diagnose wave breaking based on large-scale flow variables.

The simulation results have been used to produce a regime diagram giving a description of the wave breaking behaviour in Richardson number–dimensionless mountain height parameter space. By selecting flow overturning occurrence as a discriminating factor, it was possible to split the regime diagram into sub-regions with and without wave breaking.

When mountain waves break, the associated convective instability leads to turbulence generation (which is one of the known forms of Clear Air Turbulence, also known as CAT). Thus, regions within the simulation domain where wave breaking and the development of CAT are expected have been identified. The extent of these regions increases with terrain elevation and background wind shear intensity.

Analysis of the model output, supported by theoretical arguments, suggest the existence of a link between wave breaking and the relative orientations of the incoming wind vector and the horizontal velocity perturbation vector. More specifically, in a wave breaking event, due to the effect of critical levels, the background wind vector and the wave-number vector of the dominant mountain waves are perpendicular. It is shown that, at least for the wind profile employed in the present study, this corresponds to a situation where the background wind vector and the velocity perturbation vector are also approximately perpendicular.

Key Words: Gravity waves, Wave breaking, Turbulence, 3D mountains, Directional shear

Received . . .

1. Introduction

The role of orographic gravity waves, or mountain waves, in weather and climate studies is widely recognized. These waves are generated when stably stratified air masses are lifted by flow over orography. Under favourable atmospheric conditions (in terms of atmospheric stability and wind speed profiles) and lower boundary conditions (imposed by the terrain elevation), mountain waves can break. Breaking waves affect the atmospheric circulation by deposition of wave momentum into the mean flow (Lilly and Kennedy 1973), which manifests itself as a drag force acting on the atmosphere. Wave breaking also poses a serious safety hazard to aviation through Clear-Air Turbulence (CAT) generation (Lilly 1978). This form of CAT can be quite severe and usually occurs at altitudes relevant for general and commercial aviation (i.e., within the troposphere and lower stratosphere) (Sharman *et al.* 2012b). However, presently, techniques to forecast CAT generated by mountain wave breaking are still not sufficiently accurate (Sharman *et al.* 2012a).

While the conditions for mountain wave breaking for a constant or unidirectionally sheared background wind have been studied in substantial detail, the more common case of wave breaking occurring in winds that turn with height (i.e., with directional shear) remains incompletely understood.

Directional shear flows are ubiquitous in the atmosphere. Throughout most of the mid-latitudes, the low-level shear vector turns anticyclonically with height (Lin 2007). Directional shear is often linked to thermal advection through the thermal wind relation. Indeed, in presence of a temperature gradient, a geostrophically-balanced flow will align itself with the isotherms

by turning clockwise with height in the case of warm advection, and counter-clockwise with height in the case of cold advection (Holton and Hakim 2012). Directional wind shear can also be associated with long-period inertia-gravity waves (Mahalov *et al.* 2009). An example of observed mountain wave breaking in the presence of directional wind shear over the French Alps was reported by Doyle and Jiang (2006).

In the simpler case of an unsheared flow over 2D orography, wave breaking conditions are essentially controlled by the value of the dimensionless mountain height $N_0 H/U$ (where H is the mountain height, N_0 is the Brunt-Väisälä frequency and U is the wind speed of the background flow). Linear theory breaks down when $N_0 H/U$ is large, but it can be used to obtain a rough estimate of the critical dimensionless mountain height for which the streamlines become vertical (i.e., flow overturning occurs), and hence wave breaking is expected. This critical value is $N_0 H/U = 1$ for hydrostatic flow with the Boussinesq approximation over a bell-shaped ridge, defining an absolute limit of applicability of the linear solutions, since the velocity perturbation u' is then no longer small, but has the same magnitude as the background flow velocity U. As shown in previous studies (Baines (1998), Ambaum and Marshall (2005)), it is possible to identify different flow types based on the value of the dimensionless mountain height $N_0 H/U$ and the mountain aspect ratio H/a (where a is the mountain half-width), for which the magnitudes of u' and U become comparable, leading to flow separation. In particular, for a mountain aspect ratio $H/a \ll 1$ (i.e., hydrostatic flow) and a $N_0 H/U$ larger than 1, flow separation occurs just downstream the mountain (post-wave separation).

Long (1953) developed a non-linear theory for similar 2D flows (featuring a linear equation but a nonlinear lower boundary condition), which predicts the critical mountain height for hydrostatic flow overturning over a bell-shaped ridge to be instead $N_0 H/U = 0.85$ (Miles and Huppert 1969). This value limits Long's model validity, not because of the magnitude of the flow perturbation (which could be arbitrary large), but because wave breaking is expected beyond this threshold, which violates the steady-state assumption.

Smith (1989) used linear theory to study stratified flow past a 3D isolated mountain. For an unsheared and hydrostatic flow with the Boussinesq approximation over a mountain of sufficiently high amplitude, linear theory predicts two stagnation points (one on the windward slope of the mountain and the other one above the mountain top). Flow stagnation aloft is a precursor to overturning of isentropic surfaces (which replace streamlines in 3D flow) and therefore wave breaking. Smith formulated a condition for flow stagnation in terms of a critical dimensionless mountain height, above which the flow splits at the surface or overturns aloft. For the unsheared cases he considered, this only depends on the horizontal aspect ratio of the mountain (which controls directional dispersion effects).

As we consider more realistic flow setups (no Boussinesq approximation, and wind profiles with vertical shear, but still approximately hydrostatic conditions), there are basically two additional physical mechanisms that contribute to mountain wave breaking apart from the orography amplitude: the decay of density with height and vertical shear in the wind profile.

The effect of the decay of density with height is fairly straightforward, relying on conservation of the momentum flux as the wave propagates upward (in accordance with the theorem formulated by Eliassen and Palm (1960)), whereby a decrease in density corresponds to an increase in the amplitude of the wave velocity perturbations. This mechanism is currently included in drag parametrizations, based on the theory developed by McFarlane (1987).

The effect of vertical wind shear in unidirectionally sheared flows is also fairly straightforward. When the background wind decreases to zero, in what is usually termed a critical level, this always causes, no matter how small the waves are at their source, an indefinite increase in the wave amplitude as they approach the critical level, which necessarily results in flow overturning (Nappo 2012). This mechanism, which is associated with a divergence of the wave momentum flux, is also incorporated in current drag parametrizations (e.g. Lott and Miller (1997)).

The much more complicated case of a wind with directional shear over a 3D mountain was first addressed theoretically by Broad (1995) and Shutts (1995). Whereas in unsheared flows the surface amplitude of the wave excited by the mountain is the sole responsible for fulfilment of the wave breaking condition, and in unidirectional sheared flows critical levels affect the whole wave spectrum at once at discrete heights, always leading to wave breaking, in directional shear flows the situation is more complicated. Turning of the background wind vector with height creates a continuous distribution of critical levels in the vertical where the wave energy is absorbed into the background flow, which only affect one wave-number in the wave spectrum at a time (i.e., at each level). This effect is currently not represented in drag parametrizations, although its role in determining mountain wave drag has been pointed out in several studies (e.g. Teixeira and Miranda (2009), Xu *et al.* (2012), Xu *et al.* (2013)).

While wave breaking is thought to occur also in winds that turn with height (Broad 1995), it is weaker and distributed vertically. Since the background flow no longer needs to stagnate at critical levels, but rather is perpendicular to the affected wave-numbers, there are also indications that flow overturning may occur at considerable horizontal distances from the mountain that generates the waves (Shutts and Gadian 1999). Therefore, the distribution of critical levels and of wave breaking with height is very sensitive to the background wind profile.

In flow over a 3D mountain, with or without shear, the vertically propagating mountain waves weaken aloft because of directional dispersion associated with the spreading of the wave pattern around the mountain (if the flow is substantially non-hydrostatic additional dispersion effects arise). This decay with height, which does not exist in flow over a 2D mountain, is counteracted by the decrease of air density with height and other processes, including critical levels, which cause the wave amplitude to increase. It is the balance between all these processes that will determine the occurrence of wave breaking or not. Furthermore, in flow over 3D mountains, wave breaking is made less likely by flow splitting around the mountain near the surface. If much of the flow is diverted along the mountain flanks, the wave field aloft will weaken and wave breaking may be limited or totally suppressed (Miranda and James 1992). This is a process that occurs at high $N_0 H/U$ and is obviously absent in flow over 2D ridges.

Following previous studies (Shutts and Gadian (1999), Teixeira *et al.* (2004)), the wind profile employed here assumes that both the magnitude and the rate of rotation of the wind vector with height are constant. Even though it is not particularly realistic, this idealized wind profile can be considered a prototype of flows with directional wind shear, enabling us to isolate the effect of background shear on wave breaking and encapsulate it in a single dimensionless parameter, the Richardson number, which furthermore is constant. Teixeira *et al.* (2004) showed that the curvature of the velocity profile associated with this type of wind profile increases the surface drag. This may have implications for wave breaking, since a larger amount of momentum flux is then available to be transferred to the other flow components (mean flow or turbulence) (Teixeira and Miranda 2009).

The present study is motivated by the fact that even if the wave breaking phenomenology and mechanisms have been fairly well studied, it is still hard to predict when mountain waves will break

in directional shear flows. Results from linear theory on this phenomenon are obviously questionable, since wave breaking is an intrinsically non-linear process. So, 3D numerical simulations provide almost the only viable method to understand and predict mountain wave breaking in a systematic way.

In this paper, turbulence generation due to orographic gravity wave breaking is indirectly studied using such an approach, focusing particularly on the mechanisms by which CAT may be triggered by directional wind shear. High-resolution numerical simulations of idealized flows over a three-dimensional axisymmetric isolated mountain are carried out using the Weather Research and Forecasting model (WRF-ARW version 3.6). The aim is to diagnose the conditions for mountain wave breaking in terms of the orography elevation and wind shear, quantified by the dimensionless mountain height and the Richardson number of the background flow, respectively.

In section 2 details about the simulations, model set-up and diagnosis of wave breaking within the computational domain are presented. In section 3, results for wave breaking in directional shear flows are presented and discussed, and the section closes with an interpretation of the behaviour of the wave velocity perturbation observed in the simulations. In section 4 the main conclusions of this study are summarized.

2. Methodology

2.1. *Setup of numerical simulations*

WRF (Skamarock *et al.* 2005) is a mesoscale, non-hydrostatic, fully-compressible model whose validity in simulating mountain waves has been tested in previous studies such as Doyle (2004) and Hahn (2007). The model was used in an idealized configuration and the dynamical core only (with no parametrizations) was employed to run the simulations. The simulated flow is adiabatic (with no heat or moisture fluxes from the surface), inviscid (with no explicit diffusion allowed anywhere, and thus no Planetary Boundary Layer), and rotational effects due to the Coriolis force are neglected. The initial conditions were determined using a constant Brunt-Väisälä frequency $N_0 = 0.01\ \mathrm{s}^{-1}$, a surface potential temperature $\theta_0 =$ 293 K, a mean sea level pressure p_0 =1000 hPa and a westerly background wind $U = 10\ \mathrm{m\,s}^{-1}$ (the magnitude of the wind velocity vector is the same also for the directional wind shear simulations, where only the u and v velocity components change with height). The computational domain comprises 100 grid-points in both the x and $y-$directions, with an isotropic grid spacing $\Delta x = \Delta y = 2$ km. The lateral boundary conditions are open. The lower boundary condition is imposed by assuming a three-dimensional bell-shaped mountain with a circular horizontal cross-section, centred in the middle of the computational domain, defined by:

$$h(x,y) = \frac{H}{\left(\frac{x^2}{a^2} + \frac{y^2}{a^2} + 1\right)^{3/2}}, \qquad (1)$$

where a is the mountain half-width and H is the maximum mountain height. In order to simulate a nearly hydrostatic flow, the mountain half-width was kept fixed at 10 km in all the simulations, which corresponds to $N_0 a/U = 10$.

The model grid comprises 200 eta levels (using a terrain-following hydrostatic-pressure coordinate), with spacing near the ground of 45 m and spacing at the top of the domain, 20 km above ground level (a.g.l.), of 450 m. With such a high vertical resolution the gravity waves generated by the mountain, having a vertical wavelength of about 6 km, are everywhere well resolved (both at lower levels and at the top of the domain where the grid is coarser). An absorbing sponge layer at the top of the domain (above 15 km a.g.l.) was used to control wave reflection from the upper boundary.

The model spin-up time was estimated as 6 hours by evaluating the time evolution of the surface pressure drag. The drag attains a steady state (with an approximately constant value) roughly after that time.

A total of 35 simulations were run. Each simulation is 24-hours long and the model was set up to produce outputs with an hourly frequency. The simulations differ in degree of flow non-linearity and directional wind shear intensity. For each model run the initial conditions were modified by varying the non-dimensional mountain height $N_0 H/U$, which determines the amplitude of the orographic gravity waves at the source, and the Richardson number of the background flow $\mathrm{Ri_{in}}$, which determines the strength of the directional wind shear.

The $N_0 H/U$ parameter was gradually increased by varying the mountain height H (keeping N_0 and U constant) and the Richardson number of the incoming flow $\mathrm{Ri_{in}}$ was decreased successively by a factor of two. More specifically, the values considered for these dimensionless parameters are: $N_0 H/U =$ 0.1, 0.2, 0.5, 0.75, 1 and $Ri_{in} = \infty$, 16, 8, 4, 2, 1, 0.5 .

In general, the gradient Richardson number is defined by:

$$\mathrm{Ri} = \frac{N^2}{\left(\frac{\partial u}{\partial z}\right)^2 + \left(\frac{\partial v}{\partial z}\right)^2}, \qquad (2)$$

where N, u and v are the total Brunt-Väisälä frequency and wind velocity components (including wave perturbations). Denoting the background wind by $\mathbf{U} \equiv (u_0, v_0, 0)$, in the case of flows with no shear, $v_0 = 0$ and $u_0 = U$, which is constant with height, thus $\mathrm{Ri_{in}}$ = ∞. In the case of flows with directional shear, the u_0 and v_0 components are calculated at each model level based on $\mathrm{Ri_{in}}$, as follows:

$$u_0 = U\cos(\beta z), \qquad v_0 = U\sin(\beta z), \qquad (3)$$

where $\beta = N_0/(U\sqrt{\mathrm{Ri_{in}}})$. βz is the angle that the wind vector makes with the eastward direction (i.e., u_0 and v_0 are expressed in polar coordinates), and β is the rate of wind turning with height. By decreasing $\mathrm{Ri_{in}}$ the rate of turning increases, resulting in a stronger directional wind shear.

Note that since the model is run in an idealized configuration and the Coriolis force is neglected, the atmosphere is not geostrophically balanced and the wind shear is simply prescribed by (3), without making use of the thermal wind balance relationship.

2.2. *Calculation of Ri_{min} near the mountain*

The Richardson number provides information about the flow stability, quantifying the ratio between buoyancy forces and shearing forces. This study relies on the idea that for the simple atmospheric flows presented in the previous section, wave propagation and (when the required conditions are satisfied) the resulting wave breaking are the only reason for the modulation of Ri. The critical condition for wave breaking implies vertical streamlines: in this situation, flow overturning occurs and the local Richardson number becomes zero and then negative (when the potential temperature gradient becomes negative). In order to identify where and when wave breaking occurs in the simulation domain, the Richardson number of the output flow $\mathrm{Ri_{out}}(x,y,z)$ is calculated for each simulation at all grid points using centered finite differences. This Ri corresponds to the quasi-steady mountain wave configuration achieved after the drag stabilizes. This 3D Ri field is then analysed looking for minimum values $\mathrm{Ri_{min}}$. When these values are negative (or lower than than 0.25), turbulence generation by wave breaking (or by shear

instability) is assumed to occur in the simulation domain – although turbulence itself is not explicitly modelled at the 2 km horizontal resolution employed here.

The $\mathrm{Ri}_{\mathrm{min}}$ values calculated in the Results section below are those falling within a 'region of interest' delimited by upper, lower and lateral bounds selected taking into account physical relevance and computational resource availability considerations.

The upper limit of this region is simply dictated by the height of the bottom of the sponge layer employed in the simulations, which is 15 km. A few levels just below the sponge have been neglected to avoid numerical effects due to its proximity. The upper limit is, therefore, $z \approx 14\,\mathrm{km}$.

The lower limit is chosen to avoid unrealistic atmosphere-ground interactions that may develop in frictionless simulations. Even in a frictionless setup the nature of 3D flow near the ground (as described by Smith (1980) and, more recently, by Knight *et al.* (2015)) will lead to low Ri values near the surface, due to sinking of warm air from aloft in response to the lateral deflection of the flow streamlines (i.e. incipient flow splitting). Such low Ri values, not associated with wave propagation, are neglected by excluding in the analysis of the $\mathrm{Ri}_{\mathrm{out}}$ field the first levels above the ground that, in reality, would be located within the Planetary Boundary Layer (PBL). In order to assess which maximum height the PBL can reach in the atmospheric conditions considered in the frictionless simulations, simulations with the same setup but including a PBL parametrization (the YSU-PBL scheme) were run. The maximum PBL height reached, evaluated at the last hour of simulation (when the PBL is fully developed), was approximately 1 km. The effect of the PBL on the Richardson number was clearly recognizable by the presence of a continuous layer of low Ri which extended up to the first km of the atmosphere (not shown). A PBL height of 1 km is reasonable considering that the simulated atmosphere is stable and no surface heat fluxes exist so no thermally-driven turbulence can contribute to the PBL growth. For all the simulations run, with and without wind shear, 1 km is the lowest height used for determining $\mathrm{Ri}_{\mathrm{min}}$. Any process that occurs below this level would be changed by the presence of the PBL.

Several studies on both 2D and 3D flows (see for example Ólafsson and Bougeault (1997) and Peng and Thompson (2003)) have pointed out that the primary effect of surface friction on mountain waves is to decrease the wave amplitude by smoothing the lower boundary condition and hence making wave breaking less likely. Indeed, as Ólafsson and Bougeault (1997) first noted considering different mountain heights, and subsequently Peng and Thompson (2003) confirmed for different mountain widths, the presence of a boundary layer extends the validity of linear solutions in the free atmosphere (with which we are concerned here), by making flow over higher mountains behave as invicid flow over lower (or broader) mountains (see Peng and Thompson (2003)). Furthermore, the effect of the boundary layer depends on its depth, structure and stratification (stably stratified or convective boundary layers can interact with mountain waves in significantly different ways (Jiang and Doyle 2008)). Inviscid simulations avoid these additional complications by addressing a generic situation, which may be easily made more realistic via a suitable adjustment of the lower boundary condition.

Finally, a square region surrounding the mountain, corresponding to 50 km to the east, west, north and south from the centre of the mountain, has been chosen as lateral limit. These lateral boundaries are applied only for the wind shear simulations. Using linear theory, Shutts (1998) demonstrated the existence of a so-called 'asymptotic wake' trailing away from the mountain in directional shear flows. This flow structure is due to the presence of a component of the wind parallel to the wave phase lines, which causes the wave energy to be advected indefinitely away from the mountain. In numerical simulations, this translates into a wave field that extends out of the computational domain. As a consequence, wave breaking events can often be detected at the edge of the domain. Trying to contain the entire wave field into the simulation domain would require increasing considerably its size and the associated computational costs. Even so, the robustness of the results would not be guaranteed because this asymptotic wake seems to be able to extend indefinitely. Thus, the analysis of results will focus on the region surrounding the mountain where the phenomena taking place (including wave breaking) could be, in realistic conditions with complex orography, clearly attributed to the presence of the mountain under consideration (and not, for example, to other nearby mountains).

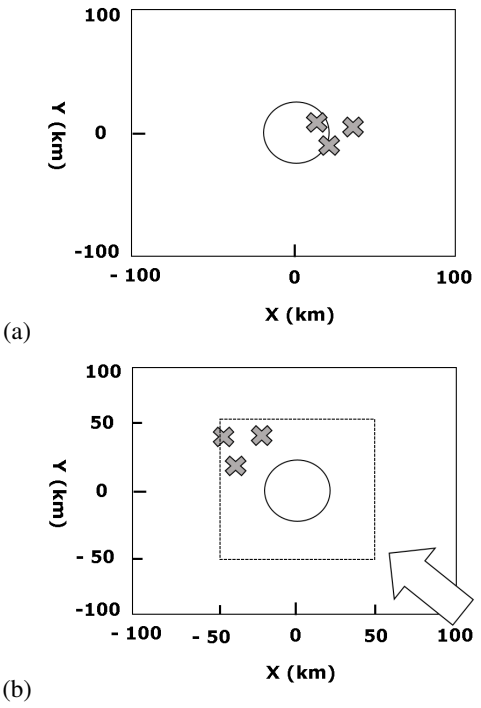

Figure 1. Sketch of the computational domain showing the location of the $\mathrm{Ri}_{\mathrm{min}}$ values (crosses) for the simulations with $\mathrm{Ri}_{\mathrm{in}} = \infty$ (a) and $\mathrm{Ri}_{\mathrm{min}} = 8$ (b), according to Tables 1 and 2. The circle represents the mountain. In (b) the arrow denotes the background wind direction at the level where wave breaking is detected, and the region within the square represents the 'region of interest' defined in section 2.2. Both sketches refer to the $N_0 H/U = 1$ simulation only.

3. Results and discussion

Within the 'region of interest' defined in the previous section, $\mathrm{Ri}_{\mathrm{min}}$ values were determined for the 35 numerical simulations carried out. Table 1 and Table 2 contain the results obtained for two representative cases: $Ri_{in} = \infty$ and $\mathrm{Ri}_{\mathrm{in}} = 8$, respectively. For each simulation the $N_0 H/U$ values used in input are specified, and the $\mathrm{Ri}_{\mathrm{min}}$ position on the horizontal and vertical grid in the output flow are shown. These results are presented using tables given the importance attached to the exact numerical value of $\mathrm{Ri}_{\mathrm{min}}$, on which some relevant considerations can be made. However, a complete overview of the results obtained in all the simulations will be provided below using a more comprehensive regime diagram.

3.1. Simulations without wind shear

Analysis of the 3D $\mathrm{Ri}_{\mathrm{out}}$ field for the no-shear case showed, as expected, that the vertical wave propagation modulates the total Richardson number of the flow, decreasing its value by increasing the wind shear and modifying the stability in some regions. All

Table 1. The $\mathrm{Ri_{min}}$ values found for the simulation with $\mathrm{Ri_{in}} = \infty$. X and Y give the horizontal position where the minimum Richardson number values occur (the mountain is located at the centre of the domain $X = 0$, $Y = 0$). The altitude in meters is also indicated.

H (m)	N_0H/U	Altitude (m)	Y (km)	X (km)	$\mathrm{Ri_{min}}$
100	0.1	2041	- 2	4	344.80
200	0.2	1577	0	6	83.04
500	0.5	1357	0	8	10.30
750	0.75	1444	0	8	3.50
1000	1	1650	0	8	1.40

Table 2. As Table 1 but for the simulation with $\mathrm{Ri_{in}} = 8$.

H (m)	N_0H/U	Altitude (m)	Y (km)	X (km)	$\mathrm{Ri_{min}}$
100	0.1	5358	50	- 24	4.65
200	0.2	5429	50	- 24	3.00
500	0.5	5642	50	- 28	0.94
750	0.75	6014	50	- 36	0.20
1000	1	6391	40	- 36	-1523.17

the minimum values are located directly above the mountain or slightly downstream, as shown by the sketch in Figure 1(a). This result is expected: mountain waves transport energy vertically. When the wave perturbations are in hydrostatic balance, this energy transport is upward directly above the mountain.

For small-amplitude mountains ($H = 100$ m, $H = 200$ m), while being perturbed by the wave, the Richardson number values are very high. For larger mountain heights ($H = 500$ m, $H = 750$ m, $H = 1$ km) the flow becomes more nonlinear and the Ri values decrease down to a minimum of 1.4 (see Table 1) for a 1 km mountain. However, for all the simulations performed, negative values of Ri were not observed, emphasizing that in the simple case of a constant background wind and stratification over an axisymmetric mountain wave breaking does not occur for $N_0H/U \leq 1$. This is in agreement with linear theory (Smith 1989), and is corroborated by the numerical simulations of Miranda and James (1992), which also indicate that beyond the narrow range of $N_0H/U > 1$ for which wave breaking does occur, the vertically propagating waves weaken due to flow splitting. Therefore, the present results are consistent with both previous numerical simulations and linear theory, although the latter was formulated by Smith using the Boussinesq approximation, and using linear solutions to study an intrinsically non-linear phenomenon such as wave breaking is questionable.

Previous studies (Smolarkiewicz and Rotunno 1989; Miranda and James 1992; Bauer *et al.* 2000) suggest that a 3D flow over an axisymmetric mountain enters a wave-breaking regime for $1 < N_0H/U < 2$. Thus, in order to induce wave breaking, additional simulations using mountain heights H of 1.25 km and 1.5 km (i.e. $N_0H/U = 1.25$ and 1.5, respectively) were run. Figure 2 shows vertical cross sections (passing through the centre of the computational domain) of the potential temperature (black solid lines) and u velocity (filled contours) for the 20th (Figure 2(a)) and 21st (Figure 2(b)) hours of the simulation for H =1.5 km. In Figure 2(a) the steepness of isentropic surfaces (which coincide with streamlines) is critical, i.e. the streamlines are vertical at a height of about 2 km, just downstream of the mountain, and in Figure 2(b) the presence of overturned streamlines implies local static instability. In this situation, waves break, and subsequently the flow becomes statically stable again (not shown). Any turbulence generation thus tends to be intermittent.

A similar flow configuration is found for the simulation performed using H =1.25 km, confirming that for $N_0H/U > 1$ wave breaking may be observed in unsheared flow, as originally found by Miranda and James (1992). The good agreement between our

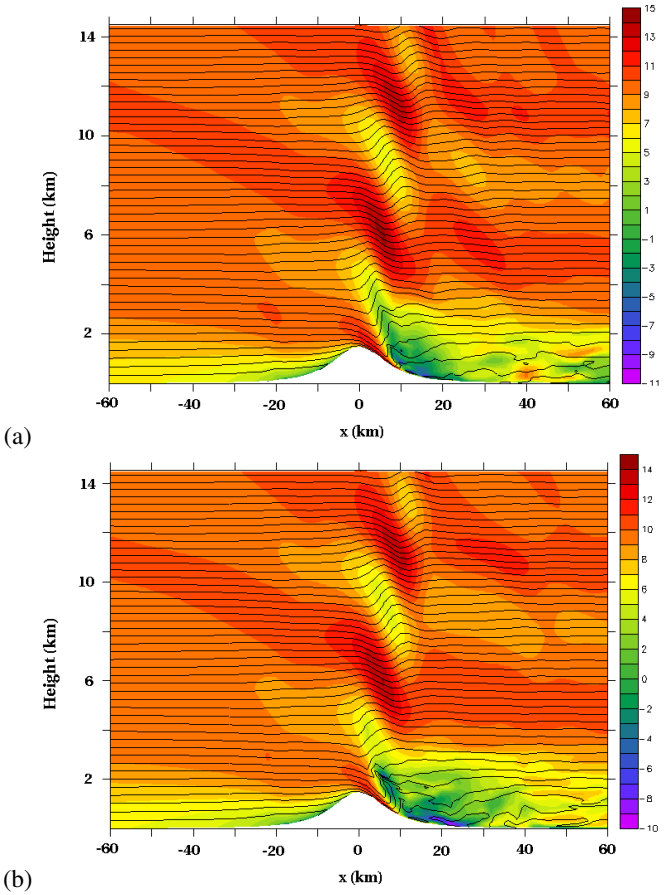

Figure 2. Flow structure for two successive model outputs in the no-shear simulation using a mountain height $H = 1.5$ km: 20th (a) and 21st (b) hours of simulation. The solid lines are isentropic surfaces (with a spacing of 1 K), the background contour field denotes the u velocity component (in $\mathrm{m\,s^{-1}}$).

results and previous theoretical and numerical studies demonstrate that the numerical setup chosen for this study is appropriate.

3.2. *Wind shear simulations*

Adding a directional wind shear to the background flow reduces the stability of the flow by decreasing the value of Ri by an amount that, if large enough, can lead alone to generation of instabilities, and hence potentially to turbulence. In real flows, a background $\mathrm{Ri_{in}} \leq 0.25$ would allow spontaneous generation of turbulence that would mask the turbulence due to wave breaking. Because of that, and also because such low values of Ri are very rare in the real atmosphere, the smallest value of $\mathrm{Ri_{in}}$ considered here is 0.5, which is still above the critical threshold value of 0.25 for which dynamic instability is expected. The largest value of $\mathrm{Ri_{in}}$, on the other hand, was chosen so that the corresponding wind shear, even if weak, is still able to affect the waves appreciably.

When mountain waves are generated, the shear due to the waves is added to the shear of the background flow and the resulting Richardson number is lower (although N is also modified). Thus, in shear flows, mountain wave propagation triggers turbulence earlier than in no-shear flows (as will be seen in more detail next). However, due to the nonlinear response of the waves to the background flow and the effect of critical levels, these processes are far from being simply additive.

A complete overview of the numerical simulation results is provided by the regime diagram shown in Figure 3. The model outputs of the last 7 hours of the simulations were analysed, looking for $\mathrm{Ri_{min}}$. In those simulations where wave breaking does not occur ($\mathrm{Ri_{out}}$ always positive) the hourly values of $\mathrm{Ri_{min}}$ are nearly constant and may vary, between an hour and the next, by only a few percent. When wave breaking is observed, in contrast,

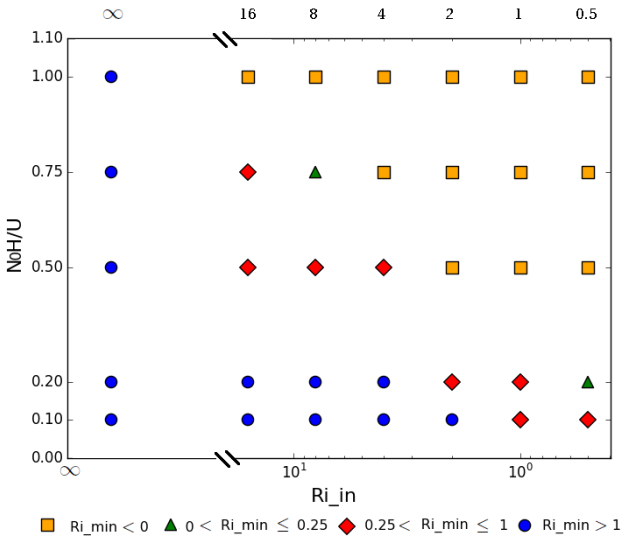

Figure 3. Regime diagram describing the nature of the flow using four categories based on the $\mathrm{Ri}_{\mathrm{min}}$ values. In the lower horizontal axis a logarithmic scale is used for $\mathrm{Ri}_{\mathrm{in}}$, however for increased readability the actual $\mathrm{Ri}_{\mathrm{in}}$ values considered are shown on the upper horizontal axis.

the $\mathrm{Ri}_{\mathrm{min}}$ values oscillate in time due to the intermittency of this process, but remain negative. In Figure 3, all the $\mathrm{Ri}_{\mathrm{min}}$ values refer to the last hour of simulation. The four categories used to build the regime diagram have been chosen in accordance with the background literature, from which it is known that the wave-turbulence interaction may begin with a dynamical instability, which leads to convective instability and then to turbulence (Nappo 2012). The four categories are: $\mathrm{Ri}_{\mathrm{min}} < 0$ indicating convective instability due to wave breaking events, $0 < \mathrm{Ri}_{\mathrm{min}} \leq 0.25$ indicating dynamic instability (potentially an index of turbulence), $0.25 < \mathrm{Ri}_{\mathrm{min}} \leq 1$ indicating a flow having kinetic energy available for turbulent mixing, and $\mathrm{Ri}_{\mathrm{min}} > 1$ indicating non-turbulent flow where no wave breaking events occur.

Whilst it is straightforward to assign a meaning to those $\mathrm{Ri}_{\mathrm{min}}$ values that are negative or large and positive, it is less obvious how to interpret the values of Ri that are small but still positive. As is well known, a Richardson number lower than 0.25 is a necessary but not sufficient condition for dynamical instability (Miles 1961). Hence, the choice of a critical Richardson number for turbulence generation is controversial, and the effective threshold value of Ri can be somewhat larger than 0.25. In fact, in atmospheric flows where the background velocity vector varies with height the energy condition for the instability threshold is less stringent than $\mathrm{Ri} < 0.25$ (Hines 1971; Turner 1973). Further, in case of finite perturbations (as the ones generated by finite amplitude gravity waves) the available kinetic energy contained in a flow with $\mathrm{Ri} < 1$ is in principle sufficient for turbulence generation (Businger 1969). As mentioned before, in the simulations presented here, no turbulent mixing is allowed. Therefore, categories 2 (triangles, $0 < \mathrm{Ri}_{\mathrm{min}} \leq 0.25$) and 3 (diamonds, $0.25 < \mathrm{Ri}_{\mathrm{min}} \leq 1$) in the regime diagram have been chosen to highlight the flows that, potentially, can evolve into turbulence.

It is also worth mentioning that flows in the regime diagram having $\mathrm{Ri} < 0.25$ can be relevant for the problem of mountain wave reflection and resonant drag enhancement. Indeed, when waves propagate from layers with larger Ri to layers with $\mathrm{Ri} \leq 0.25$, in the presence of critical levels, linear theory shows that the wave solution changes its nature and perfect wave reflection or over-reflection may occur (Lindzen and Tung 1976). If the reflected downward-travelling waves interfere constructively with the incoming upward-travelling waves, the wave amplitude, and hence the drag, may be amplified by a large factor (Lin 2007).

Analysing the regime diagram in Figure 3, we can see that whereas in the no-shear case ($\mathrm{Ri}_{\mathrm{in}} = \infty$) wave breaking does not occur ($\mathrm{Ri}_{\mathrm{min}} > 1$ always), in the shear flows considered here wave breaking is always found for a non-dimensional mountain height $N_0 H/U = 1$, no matter what $\mathrm{Ri}_{\mathrm{in}}$ is used. For $N_0 H/U = 0.75$ wave breaking is detected when $\mathrm{Ri}_{\mathrm{in}} \leq 4$, but a very small value of Ri lower than 0.25 occurs already for $\mathrm{Ri}_{\mathrm{in}} = 8$. For $N_0 H/U = 0.50$ wave breaking is present when $\mathrm{Ri}_{\mathrm{in}} \leq 2$, although $\mathrm{Ri}_{\mathrm{min}}$ is never larger than 1 for any wind shear intensity considered. It is only when assuming very small mountain heights ($N_0 H/U = 0.1$ and $N_0 H/U = 0.2$) that wave breaking is absent. However, when using a strong background wind shear (low $\mathrm{Ri}_{\mathrm{in}}$), the $\mathrm{Ri}_{\mathrm{min}}$ values obtained are small (lower than 1 or 0.25). This is, of course, consistent with the fact that we always have $\mathrm{Ri}_{\mathrm{min}} < \mathrm{Ri}_{\mathrm{in}}$.

The regime diagram therefore shows that either considering a fixed wind shear intensity of the background flow and increasing the mountain height or using a fixed $N_0 H/U$ and increasing the wind shear intensity makes the flow more likely to overturn, ultimately leading to wave breaking. By selecting flow overturning ($\mathrm{Ri}_{\mathrm{min}} < 0$) as a discriminating factor, it is possible to split the regime diagram in two sub-regions representing a non-wave-breaking flow regime and a wave-breaking regime. Regimes where the flow behaviour is less clear-cut are accounted for by the relatively narrow regions with $0 < \mathrm{Ri}_{\mathrm{min}} < 0.25$ or $0.25 < \mathrm{Ri}_{\mathrm{min}} < 1$.

It should be noticed that if the vertical axis in Figure 3 was extended up to higher values of $N_0 H/U$ the wave breaking regime would continue, including now also the no-shear case (results not shown), as discussed in the previous section. This was confirmed in a few examples, but simulations using mountain heights of 1.25 km and 1.5 km and finite $\mathrm{Ri}_{\mathrm{in}}$ were not carried out systematically because it is clear beforehand that they would also produce wave breaking. Even larger mountain heights ($N_0 H/U > 1.5$) were not considered because the flow would then enter a flow-splitting regime (Lin 2007) where wave generation aloft would be strongly attenuated or totally suppressed (Miranda and James 1992).

3.2.1. *Non-wave breaking regime*

In the absence of wave breaking, mountain waves are almost perfectly steady and the perturbation pattern associated with their propagation is stationary in time. Therefore, for those flows falling into the non-wave breaking regime in Figure 3, $\mathrm{Ri}_{\mathrm{min}}$ occurs at the points where the flow gets closest to instability. The stationary character of the solution enables one to analyse how it varies as function of the input conditions. Figure 4 shows how the $\mathrm{Ri}_{\mathrm{min}}$ values vary as a function of $\mathrm{Ri}_{\mathrm{in}}$ for a same $N_0 H/U$ value in the flows with shear. The one-to-one line represents the response that the flow would have in a perfectly linear regime, where waves are generated by an infinitesimal mountain and their perturbation of the background flow is itself infinitesimal ($\mathrm{Ri}_{\mathrm{out}} = \mathrm{Ri}_{\mathrm{in}}$). As we start to consider finite mountain heights, the simulation results show that an increase in $N_0 H/U$ corresponds to a decrease of $\mathrm{Ri}_{\mathrm{min}}$ in flows with the same background wind shear (i.e. same $\mathrm{Ri}_{\mathrm{in}}$). A base-2 logarithmic scale is used on both the horizontal and vertical axes to highlight the values of $\mathrm{Ri}_{\mathrm{in}}$ used, and also the fact that, when $N_0 H/U = 0.1$, the variation of $\mathrm{Ri}_{\mathrm{min}}$ with $\mathrm{Ri}_{\mathrm{in}}$ suggests the existence of a power law behaviour (more exactly a linear relationship). However, the $N_0 H/U = 0.1$ curve is the only one that behaves in this way. For higher values of $N_0 H/U$, the relationship between $\mathrm{Ri}_{\mathrm{min}}$ and $\mathrm{Ri}_{\mathrm{in}}$ is more complicated and the small number of data points in the cases $NH/U = 0.5$ and $NH/U = 0.75$ does not allow many conclusions to be drawn about this relationship. This small number of points is due to the fact that, in these cases, the majority of the points correspond to wave breaking situations.

A final comment on the non-wave breaking regime concerns

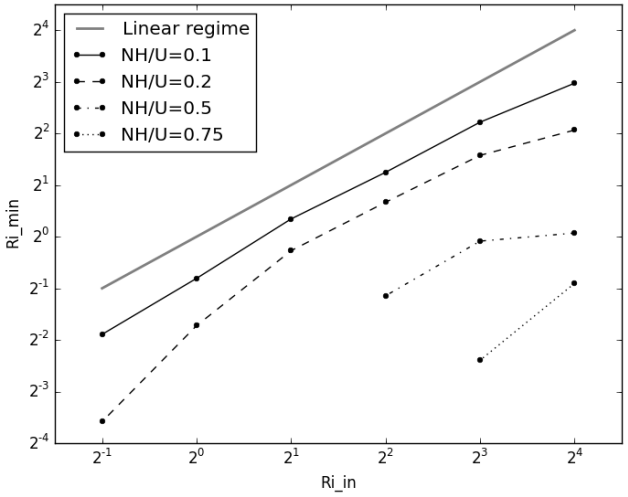

Figure 4. $\mathrm{Ri_{min}}$ for flows in the non-wave breaking regime (according to Figure 3) versus $\mathrm{Ri_{in}}$ for different N_0H/U values. On both the horizontal and vertical axes a base-2 logarithmic scale is used.

the flow category 2 (represented by triangles) that seems to be under-represented in the regime diagram of Figure 3. Only two of the considered background flow conditions ($N_0H/U = 0.75$ with $\mathrm{Ri_{in}} = 8$, and $N_0H/U = 0.2$ with $\mathrm{Ri_{in}} = 0.5$) lead the flow to have a quasi-stationary configuration with $0 < \mathrm{Ri} < 0.25$. This is partly explained by the fact that the values of N_0H/U and $\mathrm{Ri_{in}}$ have a relatively sparse sampling in the regime diagram. Taking into account more $\mathrm{Ri_{in}}$ values in the interval $[0.5, 16]$ would probably increase the number of points falling into this category. Nonetheless, this region in the flow regime is necessarily narrow. This is consistent with a previous study by Laprise and Peltier (1989), where it was shown (for a case without shear) that when the flow transitions from a situation without wave breaking to a situation with flow overturning, the Richardson number changes from being positive and larger than 0.5 to (suddenly) becoming large and negative, without taking (steady) values in the interval $[0, 0.5]$ (see their Figure 10). Therefore, a steady state mountain wave field having $0 < \mathrm{Ri} < 0.25$ may be difficult to attain, perhaps because of the onset of dynamical instability.

3.2.2. *Wave breaking regime*

The mechanism leading to wave breaking in shear flows is fundamentally different from the one acting in the no-shear case where the amplitude of the mountain is the sole responsible for

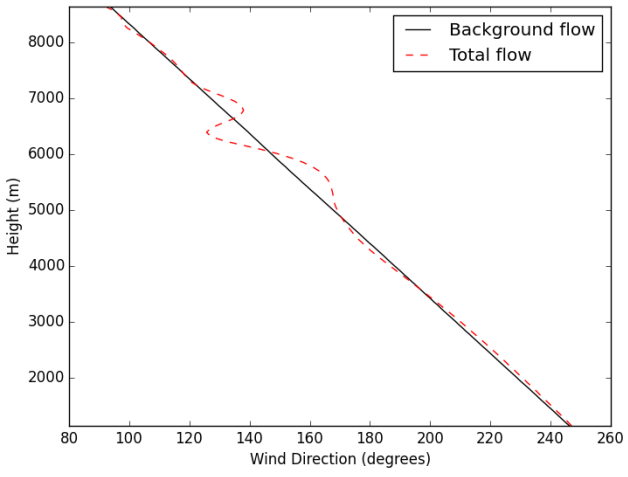

Figure 5. Variation of the wind direction with height for the simulation with N_0H/U=1 and $\mathrm{Ri_{in}}$=8. The profile includes the point where the minimum Richardson number occurs (according to Table 2).

the fulfilment of the flow overturning condition. For a no-shear flow no environmental critical levels exist, but a self-induced critical level is created where the background flow velocity $\mathbf{U}$ plus the wave velocity perturbation (u', v') add up to zero, leading to vertical streamlines (Clark and Peltier 1984). For directional shear flows, environmental critical levels are defined as the heights where the horizontal wave number vector $\boldsymbol{\kappa}_H \equiv (k, l, 0)$ is perpendicular to the background wind vector $\mathbf{U} \equiv (u_0, v_0, 0)$. When this happens ($\mathbf{U} \cdot \boldsymbol{\kappa}_H = 0$), the vertical wave number m defined in linear theory (adopting a zeroth-order Wentzel-Kramers-Brillouin (WKB) approximation) as $m = \frac{N_0(k^2+l^2)^{1/2}}{u_0k+v_0l}$ approaches infinity and the vertical wavelength $\lambda_z = 2\pi/m$ zero. As a wave packet approaches a critical level it experiences a fast oscillation ($m \to \infty$) for which the vertical velocity becomes small compared to the horizontal velocity perturbation (that actually diverges to infinity) (Shutts 1998). In these conditions the amplitude of the disturbance increases and the waves break.

Figure 5 helps to visualize what happens when a wave packet approaches a critical level. It explains the reason why the $\mathrm{Ri_{min}}$ found for $N_0H/U = 1$ and $\mathrm{Ri_{in}} = 8$ (see Table 2) is so markedly negative. Although a wave packet comprises a range of wave-numbers, that have a range of critical levels, the most active (and therefore most easily discernible) critical levels affect the wave-numbers that dominate the wave energy spectrum. The plot shows the variation of the wind direction (in degrees) with height. When the wave packet is approaching the dominant critical level, the wave amplitude increases and the background flow (solid line) is strongly modified by the wave perturbation (see dashed line). At $\sim$ 6391 m, the Richardson number approaches a highly negative value ($\mathrm{Ri_{min}}$ = -1523.17) (see Table 2) because the wind shear is made locally zero by the wave perturbation. The negative sign, on the other hand, is due to flow overturning (i.e. $N^2 < 0$). Clearly, this value is as indicative of static instability as any other negative value, since only $\mathrm{Ri_{min}} < 0$ matters for that purpose.

The aim of this work is not only to diagnose wave breaking occurrence for given background flow conditions, but also to identify regions within the simulation domain where wave breaking and the potential development of turbulence are expected. The sketch in Figure 1(b) shows the area where the $\mathrm{Ri_{min}}$ values occur for the simulations with $\mathrm{Ri_{in}}$ = 8 (based on Table 2); the arrow is the wind direction at the level where wave breaking occurs for the 1 km mountain case. Wave breaking is observed at a height of about 6.4 km where the wind is from the south-east which implies, from the definition of critical levels in directional shear flows, that the direction of the dominant wave-number vectors at that level is north-east (or south-west). The $\mathrm{Ri_{min}}$ values are found near the edge of the square 'region of interest', due to the presence of the asymptotic wake described in Section 2.

The location and values of $\mathrm{Ri_{min}}$ (such as given in Tables 1 and 2) allow us to delimit regions in the vicinity of the mountain where more detailed attention should be focused. $\mathrm{Ri_{min}}$ by itself is a poor indicator of what is going on within the simulation domain: wave breaking may be occurring simultaneously in different regions. Additionally, the temporal and spatial evolution of the flow after a wave breaking event is of particular interest. Figure 6 shows 3D plots where all the grid points for which $\mathrm{Ri_{out}} < 0.25$ are shown. The plots pertain to wind shear simulations run using a mountain height of 1 km where, according to the regime diagram in Figure 3, wave breaking always occurs. These plots can be seen as instantaneous snapshots of the flow structure at the 18th hour of simulation. The different background wind profiles for each $\mathrm{Ri_{in}}$ considered are also shown.

In order to interpret the $\mathrm{Ri_{out}} < 0.25$ fields displayed in Figure 6 in more detail, the temporal variability of Ri in a wave breaking event was analysed. For this purpose, an additional simulation using

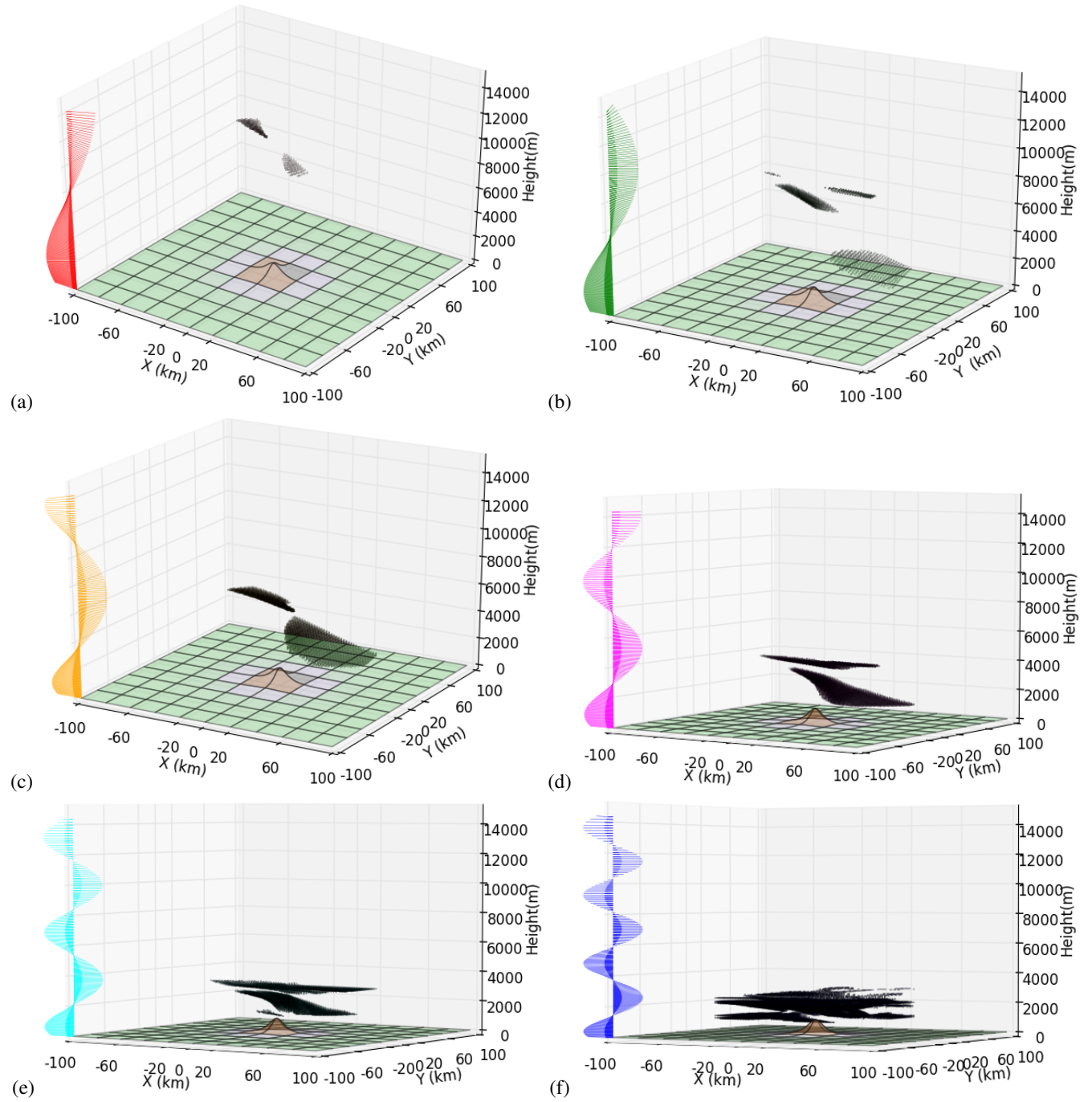

Figure 6. 3D plots showing every point in the computational domain where $\mathrm{Ri}_{\mathrm{out}} < 0.25$. The plots refer to the 18th hour of simulations and assume a $N_0 H/U = 1$ and different wind shear intensities: $\mathrm{Ri}_{\mathrm{in}}$ =16 (a), $\mathrm{Ri}_{\mathrm{in}}$ = 8 (b), $\mathrm{Ri}_{\mathrm{in}}$=4 (c), $\mathrm{Ri}_{\mathrm{in}}$ = 2 (d), $\mathrm{Ri}_{\mathrm{in}}$ = 1 (e), $\mathrm{Ri}_{\mathrm{in}}$ = 0.5 (f). The profile of vectors on the left-hand side of each plot shows the direction of the background wind as a function of height. The helical shape of the wind profile corresponds to a wind that rotates anticlockwise as z increases. At the ground the wind is always westerly, in accordance with (3).

$\mathrm{Ri}_{\mathrm{in}} = 0.5$ and a higher model output rate (i.e., 6 model outputs per hour instead of 1) was carried out. Figure 7 shows a time-series of Ri in the 6 grid-points adjacent to the one where $\mathrm{Ri}_{\mathrm{min}}$ is located at the 18th hour of the simulation, which has horizontal coordinates $X = 22$ km, $Y = -10$ km and an altitude $z \approx 3.1$ km. The time-series begins at the 7th hour of simulation (the first 6 hours have been excluded because they correspond to the model spin-up time), and data are plotted every 10 minutes.

The purpose of Figure 7 is to point out that for each grid-point, after the first wave breaking event has taken place (the first time Ri drops below 0), Ri keeps oscillating between negative and positive values. Additionally, Ri remains roughly between 0 and 0.25 both before and after wave breaking periods. The shaded regions in the 3D plots of Figure 6 therefore presumably represent locations where waves are at different stages of their intermittent breaking process, including waves which are breaking ($\mathrm{Ri} < 0$), about to break, or have already broken ($0 < \mathrm{Ri} < 0.25$). When mountain waves break the associated convective instability can lead to turbulence generation (known as Clear Air Turbulence or CAT), thus the plots in Figure 6 can been thought of as continuous regions of (potential) occurrence of mountain wave-induced CAT. The extent of these regions is variable, increasing with the background shear intensity. While for simulations using $\mathrm{Ri}_{\mathrm{in}} = 16$ localized shading is visible occupying a very small fraction of the 'region of interest', the flow topology for $\mathrm{Ri}_{\mathrm{in}} = 0.5$ is much more complex. This happens because when the shear due to waves is added to an already strong background wind shear, Ri values lower than 0.25 occur simultaneously in many vertical levels and almost everywhere across the horizontal plane. An important aspect is that, for stronger background shear, $\mathrm{Ri} < 0.25$ regions, and the $\mathrm{Ri}_{\mathrm{min}}$ values embedded in them, occur at lower levels. This means that, the stronger the directional shear

is, the faster (or, more exactly, the lower down) the wave energy is dissipated, preventing wave breaking at higher levels. This is due to the greater density of critical levels, which leads to more concentrated wave amplification, breaking, and subsequent dissipation, as will be detailed below.

The definition of critical level ($\mathbf{U} \cdot \boldsymbol{\kappa}_H = 0$) implies that, in directional shear flows where the wind turns with height continuously, all levels are critical levels. Unlike mountain waves generated by a sinusoidal terrain corrugation, orographic gravity waves excited by an isolated mountain do not have a single forcing wave-number, but rather a full spectrum of waves, with a range of wave-numbers pointing in all directions (Nappo 2012). When the wind turns with height there will always be a wave-number vector perpendicular to the wind direction at that level. However, in a wave breaking event we can assume that only the most energetic wave-numbers (associated with the largest wave amplitudes) are able to dominate the behaviour of the entire wave packet and cause wave breaking. The other less energetic wave-numbers can still change the background flow but they will not contribute as importantly to wave breaking (as shown by Figure 5). Therefore, perhaps every point where wave breaking is detected within the computational domain can be seen as a point where the background wind velocity vector is perpendicular to a dominant horizontal wave-number vector.

Because of the helical wind profile employed in the simulations, in weaker shear flows (such as that with $\mathrm{Ri_{in}} = 16$) the wind vector and the (most energetic) horizontal wave-number vectors attain perpendicularity at higher levels, making wave breaking take place at high altitudes. In stronger shear flows (such as those with $\mathrm{Ri_{in}} = 1$ or 0.5), the same wind angle occurs at lower levels. Thus, fulfilment of the condition $\mathbf{U} \cdot \boldsymbol{\kappa}_H = 0$ is more probable for a major part of the wave spectrum in the lower atmosphere. For example, using $\mathrm{Ri_{in}} = 16$ the wind changes from westerly at the ground to easterly at the bottom of the sponge layer (14 km). Considering a stronger wind shear, for example $\mathrm{Ri_{in}} = 1$, the same change in wind direction occurs over the lowest 3 km of the atmosphere. Since the wave energy is likely to be dissipated by wave breaking at the lowest critical levels the waves encounter (for low Ri, there may be multiple critical levels, as pointed out by Teixeira and Yu (2014)), at greater altitudes nearly all the wave energy has already been dissipated.

To conclude, we emphasize that the flow topology displayed in Figure 6 was found to be relatively insensitive to changes in both vertical and horizontal resolutions. Sensitivity tests using a horizontal resolution of 1 km instead of 2 km, and 400 model vertical levels instead of 200, were carried out for $\mathrm{Ri_{in}} = 16$ and 1 (weak and strong shear, respectively). In these simulations, the $\mathrm{Ri_{out}} < 0.25$ field, which characterizes regions of potential flow instability (not shown), had mostly the same distribution as in Figure 6, being only marginally affected by changes in resolution. These sensitivity tests corroborated that the resolution adopted in the present study seems appropriate to represent the major physical processes taking place in the simulation domain.

3.3. *A possible wave breaking diagnostic*

Although there is no immediate way to evaluate the dominant wave-number vectors in the mountain wave field (a spectrum would have to be computed), a joint qualitative analysis of the flow structure and of the background wind profile for the cases shown in Figure 6 suggests that these wave-number vectors (k,l) are roughly aligned with the corresponding horizontal velocity perturbation vectors (u',v'). Since the dominant wave-number vector and the background wind vector (u_0, v_0) are approximately perpendicular at each height (due to critical levels), this is equivalent to (u_0, v_0) and (u', v') also being perpendicular. This

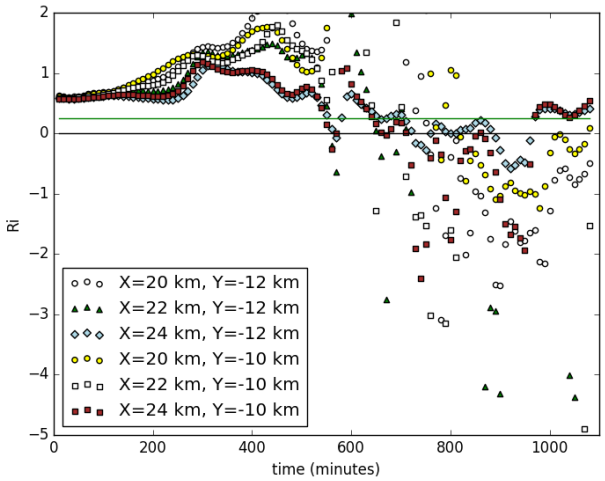

Figure 7. Time-series of the Richardson number evaluated at six grid-points adjacent to the one where, according to the $\mathrm{Ri_{out}}$ field, wave breaking occurs in the simulation with $N_0 H/U = 1$ and $\mathrm{Ri_{in}} = 0.5$. The coordinates X, Y or each point are shown. For all the considered points $z \approx 3100$ m.

behaviour was detected both in weak and in strong shear flows.

In Figure 8(a) and 8(c) two horizontal cross-sections of the wind field for the simulations with $\mathrm{Ri_{in}} = 16$ and $\mathrm{Ri_{in}} = 1$ at the 18th hour of simulation are shown. The cross-sections are taken at the model levels where, according to the analysis carried out in Figure 6, wave breaking ($\mathrm{Ri_{out}} < 0$) occurs. The regions where $\mathrm{Ri_{out}} \leqslant 0.25$ are shown by $\mathrm{Ri_{out}}$ contour lines. The magnitude of the velocity perturbation vector (u',v') is shown by the background contours. The black vectors are the background wind and the red thick vectors are the wave velocity perturbation (calculated by subtracting the background wind from the total flow).

In Figure 8(a) the branch of maximum horizontal velocity perturbation elongated to the north-west, where the background wind vector and the velocity perturbation vectors become nearly perpendicular, coincides partially with the shape of the lowest shaded region displayed in Figure 6(a) (corresponding to the $\mathrm{Ri_{out}}$ contours in the cross-section). In fact, both shaded regions in Figure 6(a) extend vertically, therefore corresponding to several model levels. The map in Figure 8(a) (at $z \approx 7$ km) contains only some of the points belonging to the lowest region. Except for the aforementioned elongated region, it is clear that elsewhere in the computational domain the wave velocity perturbation is very small and does not modify the background flow appreciably (whose vectors then coincide with those of the total flow). The same behaviour is observed for the strong wind shear case (Figure 8(c)), where departing from the middle of the computational domain towards the north-west, a region where the wave velocity perturbation becomes large and almost perpendicular to the background wind is visible. This region coincides with part of the lower boundary of the main shaded region displayed in Figure 6(e), at a height of about 2 km.

Both in Figure 8(a) and 8(c), other locations where (u_0, v_0) and (u',v') are almost perpendicular and the wave perturbation is large can be detected. These locations lie outside the $\mathrm{Ri_{out}} = 0.25$ contour, but still within the elongated region in Figure 8(a) corresponding to the maximum velocity perturbation, and at the south-east edge of the computational domain in Figure 8(c). Since at these locations $\mathrm{Ri_{out}}$ is higher than 0.25 but still small, as shown in Figure 8(b) and 8(d), this may mean that while being able to perturb the background flow, the wave amplitude is not large enough to induce dynamic instability.

The effective angle that the velocity perturbation vectors form with the background wind vector is shown in Figure 8(b) and 8(d). The dashed contour lines are a selected range of contour levels with values around 90 degrees, and in the background the $\mathrm{Ri_{out}}$

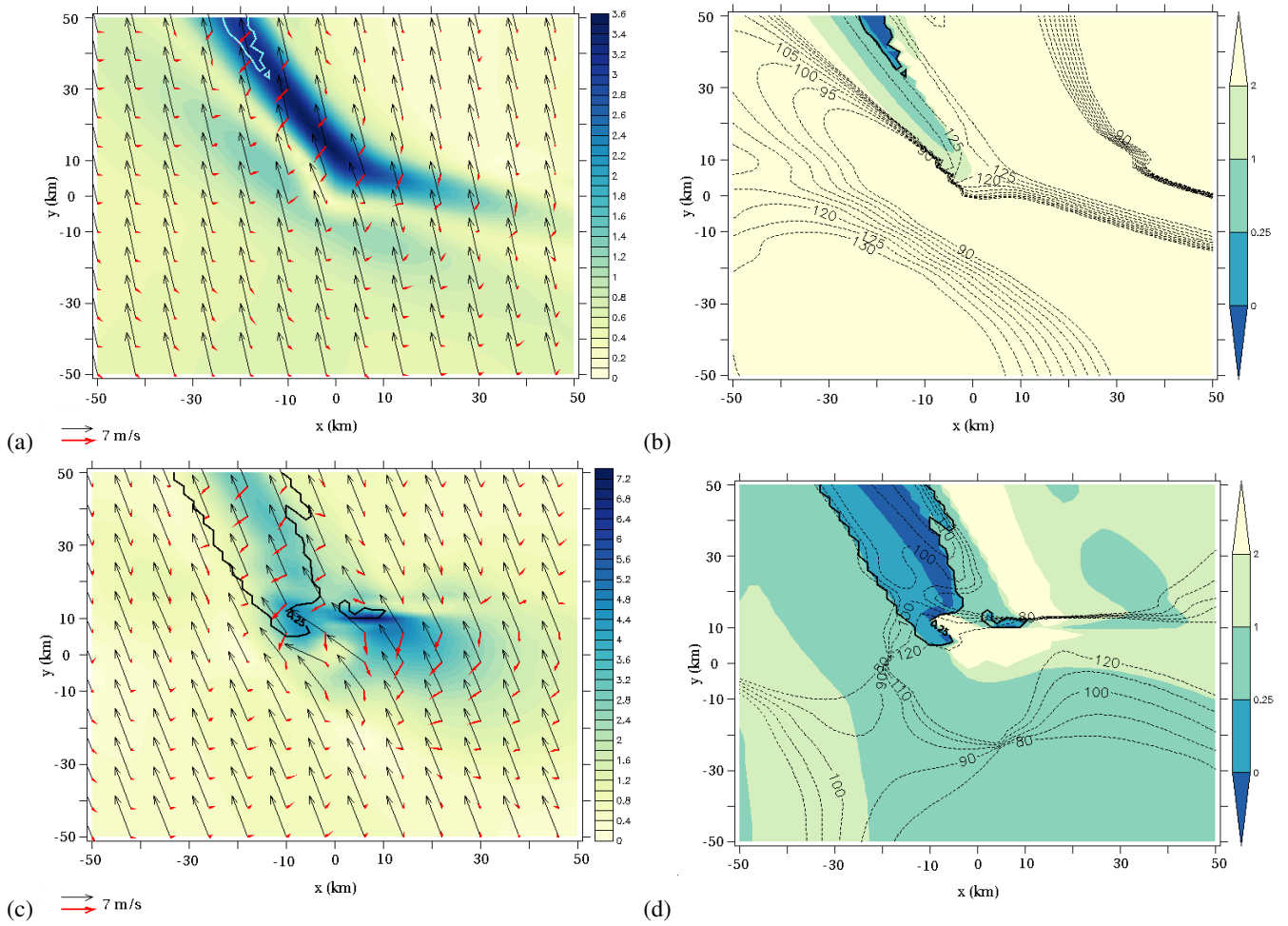

Figure 8. Horizontal cross-sections of the wind field, (a) and (c), and $\mathrm{Ri_{out}}$, (b) and (d), for the simulations with $\mathrm{Ri_{in}} = 16$ ((a) and (b)), $\mathrm{Ri_{in}} = 1$ ((c) and (d)) at the 18th hour of simulation. The cross-sections are taken at an altitude of about 7 km ((a) and (b)) and 2 km ((c) and (d)). In (a) and (c), on the background, the magnitude of the velocity perturbation vector (u',v') (in $\mathrm{m\,s^{-1}}$) is shown. The thick contour lines (white in (a), black in (c)) denote $\mathrm{Ri_{out}} = 0.25$. The black vectors are the background wind and the red thick vectors are the velocity perturbation. In (b) and (d), on the background, the $\mathrm{Ri_{out}}$ field is shown. All the $\mathrm{Ri_{out}}$ values higher than 2 and lower than 0 are represented by the same color. The dashed contour lines represent the angle between the background wind vector and the velocity perturbation vector. The thick contour lines again correspond to $\mathrm{Ri_{out}} = 0.25$.

field is shown. As observed in Figure 8(a) and 8(c), where the velocity perturbation is large and Ri $\leqslant$ 0.25 the angle between the two vectors tends to be a right angle, but it can vary between 80 and 130 degrees. Other areas within the computational domain where the two vectors make an angle roughly between 80 and 130 degrees can be detected, but in these areas the wave perturbation is small, hence it would be questionable to attach any significance to them.

These preliminary findings, based on a simple visual inspection of the Ri and wind velocity vector fields, contribute to improve our understanding of the flow structure displayed in Figure 6. They suggest a link between the orientation of the velocity perturbation vector and the background wind vector in high-amplitude wave regions, which is confirmed by a mathematical argument based on linear theory, presented next.

For hydrostatic, adiabatic, 3D, frictionless flow without rotation, the Taylor-Goldstein equation, which governs the behaviour of mountain waves, takes the form (Nappo 2012):

$$\frac{d^2\widehat{w}}{dz^2} + \left[\frac{(k^2+l^2)N^2}{(ku_0+lv_0)^2} - \frac{ku_0''+lv_0''}{ku_0+lv_0}\right]\widehat{w} = 0, \qquad (4)$$

where $\widehat{w}$ is the Fourier transform of the vertical velocity, and the primes denote differentiation with respect to z.

The Fourier transforms of the horizontal velocity perturbations are given by (Nappo 2012):

$$\widehat{u}(k,l,z) = \frac{ik}{k^2+l^2}\left[\frac{l\widehat{w}(lu_0'-kv_0')}{k(ku_0+lv_0)} + \frac{\mathrm{d}\widehat{w}}{\mathrm{d}z}\right], \qquad (5)$$

$$\widehat{v}(k,l,z) = \frac{-il}{k^2+l^2}\left[\frac{k\widehat{w}(lu_0'-kv_0')}{l(ku_0+lv_0)} - \frac{\mathrm{d}\widehat{w}}{\mathrm{d}z}\right]. \qquad (6)$$

Note that the second terms within the square brackets in (5)-(6) correspond to a vector that is parallel to the horizontal wave-number vector (k,l), whereas the first terms correspond to a vector that is perpendicular to (k,l). In shear flows, the solution to (4) may be expressed as:

$$\widehat{w} = \widehat{w}(z=0)\mathrm{e}^{i\int m(z)\mathrm{d}z}. \qquad (7)$$

Substituting (7) into (5)-(6) and adopting a zeroth-order WKB approximation, (5) and (6) become:

$$\widehat{u}(k,l,z) = \frac{ik\widehat{w}}{k^2+l^2}\left[\frac{l(lu_0'-kv_0')}{k(ku_0+lv_0)} - i\frac{N_0(k^2+l^2)^{1/2}}{ku_0+lv_0}\right], \qquad (8)$$

$$\widehat{v}(k,l,z) = \frac{-il\widehat{w}}{k^2+l^2}\left[\frac{k(lu_0'-kv_0')}{l(ku_0+lv_0)} + i\frac{N_0(k^2+l^2)^{1/2}}{ku_0+lv_0}\right], \qquad (9)$$

where $m = N_0(k^2+l^2)^{1/2}/(ku_0+lv_0)$ is the same expression for m as in the constant wind case, but where u_0 and v_0 vary with height because of directional shear. The WKB approximation assumes that the background flow changes slowly with z compared to the vertical wavelength of the waves. A slowly varying medium implies a slowly varying vertical wave-number, which allows us to approximate m as described above. Contrary to what one may expect, the WKB approximation is still valid in

flows with a fairly low Richardson number, as shown by Teixeira *et al.* (2004) and Teixeira and Miranda (2009).

At a critical level $ku_0 + lv_0 = 0$, which suggests that both the terms within the brackets in (8)-(9) would diverge to infinity. However, the helical wind profile described by (3) implies that

$$u_0' = -U\sin(\beta z)\beta = -\beta v_0\ , \quad v_0' = U\cos(\beta z)\beta = \beta u_0, \quad (10)$$

and substituting $lu_0' - kv_0' = -\beta(ku_0 + lv_0)$ into the numerators of the first terms on the right-hand side of (8) and (9), the equations for $\widehat{u}$ and $\widehat{v}$ become:

$$\widehat{u}(k,l,z) = \frac{-il\beta\widehat{w}}{k^2+l^2} + \frac{k\widehat{w}}{k^2+l^2}\frac{N_0(k^2+l^2)^{1/2}}{ku_0+lv_0}, \quad (11)$$

$$\widehat{v}(k,l,z) = \frac{ik\beta\widehat{w}}{k^2+l^2} + \frac{l\widehat{w}}{k^2+l^2}\frac{N_0(k^2+l^2)^{1/2}}{ku_0+lv_0}. \quad (12)$$

This shows that at critical levels ($ku_0 + lv_0 = 0$) the second terms on the right-hand side are the only ones that diverge to infinity, and therefore are overwhelmingly dominant. Under these conditions, the $(\widehat{u}, \widehat{v})$ vector is parallel to the wave-number vector $(k,\ l)$. Although $\widehat{u}$ and $\widehat{v}$ are the Fourier transforms of the physical u' and v' perturbation velocities, and thus contribute to u' and v' from a range of wave-numbers, their contribution is dominant at critical levels, where $(k,l)\cdot(u_0, v_0) = 0$, because of this divergent behaviour. Hence the condition that $(\widehat{u}\ , \widehat{v})$ and (k,l) are parallel at critical levels can be translated in physical space into a condition stating that $(u',\ v')$ and $(u_0,\ v_0)$ are approximately perpendicular, which explains what can be seen in Figure 8.

Note that considering a series expansion of the vertical wave-number up to second- or third-order in the WKB approximation in (7), as done by Teixeira *et al.* (2004) and Teixeira and Miranda (2009), would not add much to the present analysis or affect the conclusions inferred therefrom. This power series can be expressed as the leading zeroth-order term multiplyed by 1 plus higher-order corrections that have no singularities. Hence the singular behaviour of the whole series at critical levels can be inferred correctly using only the zeroth-order term. Furthermore, inclusion of non-hydrostatic effects in the WKB solution is not physically justified, since mountain waves are perfectly hydrostatic at critical levels, as noted by Grubišić and Smolarkiewicz (1997).

4. Summary and conclusions

In this paper orographic gravity wave breaking in flows with directional wind shear has been investigated. A set of numerical simulations were performed to study wave breaking using orography and wind profiles with a common idealized form, but varying terrain elevations and shear intensities, respectively. The numerical simulation results were summarized in a regime diagram classifying the flow behaviour. In no-shear flows, wave breaking was observed only for dimensionless mountain heights $N_0H/U > 1$, as found by previous authors.

In directional shear flows, for the values of $\mathrm{Ri_{in}}$ considered here, wave breaking always occurs when $N_0H/U = 1$. However, for gradually stronger directional shears (lower $\mathrm{Ri_{in}}$) the critical N_0H/U for wave breaking decreases down to 0.5. Therefore, in presence of directional shear, wave breaking can occur over lower mountains than in the constant-wind case, a result that is not wholly unexpected.

When mountain waves break, the associated convective instability can lead to turbulence generation (which is one of the existing forms of CAT). In this paper, the flow topology during wave breaking events was studied in order to identify regions within the computational domain where potential CAT generation is expectable. These regions correspond to all the points in the 'region of interest' embedded in the computational domain where the Richardson number of the output flow $\mathrm{Ri_{out}}$ is lower than 0.25. As the analysis of the temporal variability of Ri revealed, these dynamical instability regions can represent waves at different stages of their intermittent breaking process, namely: waves which are breaking, about to break, or that have already broken. The flow topology inferred from the present study can be summarized as follows:

- in contrast with no-shear flows where wave breaking occurs essentially over the mountain, for the helical wind profiles with directional shear adopted in this study, the flow overturning regions are more three-dimensional and spread along the 3 spatial directions;
- increasing the strength of the directional shear (i.e., reducing the value of $\mathrm{Ri_{in}}$) leads to more numerous wave breaking events and to wider regions of (potential) turbulence generation;
- for stronger shear flows, wave breaking occurs at lower levels, and all the wave energy is dissipated within the first few kms above the ground because of the fast rate of turning of the background wind with height. However, this does not imply that a stronger directional shear produces less dangerous CAT. Indeed, in real atmospheric conditions the wind can begin to turn with height at any altitude. By changing the altitude at which the wind starts to turn, we can reasonably expect that the region of instability found near the ground in the simulations presented here will be translated upwards accordingly. However, the situation is complicated by the fact that an additional physical parameter is added to the problem: the height where the wind begins to turn. This is a possible topic for future study.

The velocity field in a wave breaking event has also been analysed. By examining the dynamics of the horizontal velocity perturbations associated with the waves in Fourier space, it was found that the Fourier transform of the horizontal velocity perturbation vector and the wave-number vector are aligned at critical levels. When transposed to physical space, this explains the approximate perpendicularity between the wave velocity perturbation vector and the background wind vector detected in the flow cross-sections. However, it was observed that the angle between the two vectors ranges from 80 to 130 degrees. A reason for this behaviour may be that at a critical level wave-numbers other than the dominant one can still play a role in determining the orientation of the velocity perturbation vector, especially if the energy of the waves at the wave-number meeting a critical level is especially low. This approximate perpendicularity could in principle be used as a diagnostic for CAT forecast in directional shear flows. Indeed, looking at the orientation of the (u',v') vector is much easier than detecting where the most energetic wave components have critical levels, which entails the calculation of spectra.

Although the validity of this diagnostic is supported by a theoretical argument, its generality and applicability to real flows must be tested. Concerning the generality of the result, although the physical interpretation presented in Section 3.3 relies crucially on the form of the helical wind profile (3), we can expect it to hold approximately for any wind profile characterized by a relatively large background Richardson number. This is because the ratio between the second and the first term in (8) and (9) scales with $\mathrm{Ri_{in}^{1/2}}$. Therefore, even without considering a specific wind profile we expect the second term to dominate for large $\mathrm{Ri_{in}}$. Note, however, that this is a weaker criterion than the one used in Section 3.3, since it does not rely on singular behaviour (for which a term is infinitely larger than the other). Further clarification of this issue

would require additional numerical simulations, which are beyond the scope of this paper.

Concerning the applicability of the suggested diagnostic to real flows, difficulties may arise from the need to isolate the background flow from the total flow containing the wave perturbation. For this purpose, the wind field measured upstream of the mountain or averaged over the surrounding area may be used. It may also be challenging to distinguish between flow regions where the perpendicularity of the vectors is a signature of wave breaking and regions where this does not happen. Probably, an additional condition, involving the magnitude of the flow perturbation, will be necessary.

It is worth mentioning that developing methods to diagnose wave breaking without relying on the use of the Richardson number is a major goal for mountain wave CAT forecasting (Sharman *et al.* 2012b). While in the idealized simulations presented in this paper wave propagation is the only reason for the modulation of Ri, in real conditions Ri is a noisy variable, influenced by small-scale flow structures, displaying a large vertical-scale dependence. Even a flow with $\mathrm{Ri} > 1$ can be turbulent if this parameter is estimated at sufficiently coarse resolution. In this respect, the regime diagram presented in this paper provides a way of predicting wave breaking based only on large-scale variables using the mountain height and background wind profile, thus avoiding dependence on the wave field itself.

The results presented in this paper constitute a starting point for testing the applicability of these (idealized) simulation results to real flows. Future steps would entail carrying out numerical simulations with more realistic conditions, including: realistic orography, a PBL, non-hydrostatic effects, more complicated atmospheric profiles, etc. This should allow a better understanding of CAT generated by fully 3D mountain waves and the development of more specific tools to forecast it.

Acknowledgements

M.V.G. and M.A.C.T. acknowledge the financial support of the European Commission under Marie Curie Career Integration Grant GLIMFLO, contract PCIG13-GA-2013-618016.

References

Ambaum MHP, Marshall DP. 2005. The effects of stratification on flow separation. *J. Atmos. Sci.* **62**: 2618–2625.

Baines PG. 1998. *Topographic effects in stratified flows*. Cambridge University Press.

Bauer MH, Mayr GJ, Vergeiner I, Pichler H. 2000. Strongly nonlinear flow over and around a three-dimensional mountain as a function of the horizontal aspect ratio. *J. Atmos. Sci.* **57**: 3971–3991.

Broad AS. 1995. Linear theory of momentum fluxes in 3-d flows with turning of the mean wind with height. *Q. J. R. Meteorol. Soc.* **121**: 1891–1902.

Businger JA. 1969. Note on the critical richardson number(s). *Q. J. R. Meteorol. Soc.* **95**: 653–654.

Clark TL, Peltier WR. 1984. Critical level reflection and the resonant growth of nonlinear mountain waves. *J. Atmos. Sci.* **41**: 3122–3134.

Doyle J, Jiang Q. 2006. Observations and numerical simulations of mountain waves in the presence of directional wind shear. *Q. J. R. Meteorol. Soc.* **132**: 1877–1905.

Doyle JD. 2004. Evaluation of topographic flow simulations from coamps and wrf. In: *20th Conference on Weather Analysis and Forecasting/16th Conference on Numerical Weather Prediction*.

Eliassen A, Palm E. 1960. On the transfer of energy in stationary mountain waves. *Geofys. Publ.* **22**: 1–23.

Grubišić V, Smolarkiewicz PK. 1997. The effect of critical levels on 3d orographic flows: linear regime. *J. Atmos. Sci.* **54**: 1943–1960.

Hahn DC. 2007. Evaluation of wrf performance for depicting orographically-induced gravity waves in the stratosphere. Technical report, DTIC Document.

Hines CO. 1971. Generalizations of the richardson criterion for the onset of atmospheric turbulence. *Q. J. R. Meteorol. Soc.* **97**: 429–439.

Holton JR, Hakim GJ. 2012. *An introduction to dynamic meteorology*. Academic press.

Jiang Q, Doyle JD. 2008. On the diurnal variation of mountain waves. *J. Atmos. Sci.* **65**: 1360–1377.

Knight H, Broutman D, Eckermann SD. 2015. Integral expressions for mountain wave steepness. *Wave Motion* **56**: 1–13.

Laprise R, Peltier WR. 1989. On the structural characteristics of steady finite-amplitude mountain waves over bell-shaped topography. *J. Atmos. Sci.* **46**: 586–595.

Lilly DK. 1978. A severe downslope windstorm and aircraft turbulence event induced by a mountain wave. *J. Atmos. Sci.* **35**: 59–77.

Lilly DK, Kennedy PJ. 1973. Observations of a stationary mountain wave and its associated momentum flux and energy dissipation. *J. Atmos. Sci.* **30**: 1135–1152.

Lin YL. 2007. *Mesoscale dynamics*. Cambridge University Press.

Lindzen RS, Tung KK. 1976. Banded convective activity and ducted gravity waves. *Mon. Wea. Rev.* **104**: 1602–1617.

Long RR. 1953. Some aspects of the flow of stratified fluids: I. a theoretical investigation. *Tellus* **5**: 42–58.

Lott F, Miller MJ. 1997. A new subgrid-scale orographic drag parametrization: Its formulation and testing. *Q. J. R. Meteorol. Soc.* **127**: 101–127.

Mahalov A, Moustaoui M, Nicolaenko B. 2009. Three-dimensional instabilities in non-parallel shear stratified flows. *Kinetic and Related Models* **2**: 215–229.

McFarlane NA. 1987. The effect of orographically excited gravity wave drag on the general circulation of the lower stratosphere and troposphere. *J. Atmos. Sci.* **44**: 1775–1800.

Miles JW. 1961. On the stability of heterogeneous shear flows. *J. Fluid Mech.* **10**: 496–508.

Miles JW, Huppert HE. 1969. Lee waves in a stratified flow. part 4. perturbation approximations. *J. Fluid Mech.* **35**: 497–525.

Miranda PMA, James IN. 1992. Non-linear three-dimensional effects on gravity-wave drag: Splitting flow and breaking waves. *Q. J. R. Meteorol. Soc.* **118**: 1057–1081.

Nappo CJ. 2012. *An introduction to atmospheric gravity waves, 2nd ed.* Academic Press.

Ólafsson H, Bougeault P. 1997. The effect of rotation and surface friction on orographic drag. *J. Atmos. Sci.* **54**: 193–210.

Peng MS, Thompson WT. 2003. Some aspects of the effect of surface friction on flows over mountains. *Q. J. R. Meteorol. Soc.* **129**: 2527–2557.

Sharman RD, Doyle JD, Shapiro MA. 2012a. An investigation of a commercial aircraft encounter with severe clear-air turbulence over western greenland. *J. Appl. Meteor. Climatol.* **51**: 42–53.

Sharman RD, Trier SB, Lane TP, Doyle JD. 2012b. Sources and dynamics of turbulence in the upper troposphere and lower stratosphere: A review. *Geophys. Res. Lett.* **39**: L12 803.

Shutts G. 1995. Gravity-wave drag parametrization over complex terrain: The effect of critical-level absorption in directional wind-shear. *Q. J. R. Meteorol. Soc.* **121**: 1005–1021.

Shutts GJ. 1998. Stationary gravity-wave structure in flows with directional wind shear. *Q. J. R. Meteorol. Soc.* **124**: 1421–1442.

Shutts GJ, Gadian A. 1999. Numerical simulations of orographic gravity waves in flows which back with height. *Q. J. R. Meteorol. Soc.* **125**: 2743–2765.

Skamarock WC, Klemp JB, Dudhia J, Gill DO, Barker DM, Wang W, Powers JG. 2005. A description of the advanced research wrf version 2. Technical report, DTIC Document.

Smith RB. 1980. Linear theory of stratified hydrostatic flow past an isolated mountain. *Tellus* **32**: 348–364.

Smith RB. 1989. Mountain-induced stagnation points in hydrostatic flow. *Tellus* **41A**: 270–274.

Smolarkiewicz PK, Rotunno R. 1989. Low froude number flow past three dimensional obstacles. part 1: Baroclinically generated lee vortices. *J. Atmos. Sci* **46**: 1154–1164.

Teixeira MAC, Miranda PMA. 2009. On the momentum fluxes associated with mountain waves in directionally sheared flows. *J. Atmos. Sci.* **66**: 3419–3433.

Teixeira MAC, Miranda PMA, Valente MA. 2004. An analytical model of mountain wave drag for wind profiles withshear and curvature. *J. Atmos. Sci.* **61**: 1040–1054.

Teixeira MAC, Yu CL. 2014. The gravity wave momentum flux in hydrostatic flow with directional shear over elliptical mountains. *Eur. J. Mech. B - Fluids* **47**: 16–31.

Turner JS. 1973. *Buoyancy effects in fluids*. Cambridge University Press.

Xu X, Wang Y, Xue M. 2012. Momentum flux and flux divergence of gravity waves in directional shear flows over three-dimensional mountains. *J.*

Atmos. Sci. **69**: 3733–3744.

Xu X, Xue M, Wang Y. 2013. Gravity wave momentum flux in directional shear flows over three-dimensional mountains: Linear and nonlinear numerical solutions as compared to linear analytical solutions. *J. Geophys. Res-Atmos.* **118**: 7670–7681.

